Journal of Materials Chemistry A

PAPER

Cite this: J. Mater. Chem. A, 2015, 3, 23299

Polydopamine-derived porous carbon fiber/cobalt composites for efficient oxygen reduction reactions†

Jiajie Yan,[a] Hengyi Lu,[a] Yunpeng Huang,[a] Jun Fu,[c] Shuyi Mo,[c] Chun Wei,[c] Yue-E Miao*[b] and Tianxi Liu*[ab]

Received 8th August 2015
Accepted 9th October 2015

DOI: 10.1039/c5ta06217a

www.rsc.org/MaterialsA

Dopamine is an excellent and flexible agent for surface coating of various materials, with the high-concentration of amine groups serving as a facile stabilizer for some metallic nanoparticles. In this work, mesoporous composites of nitrogen-doped carbon fibers (NCFs) decorated with cobalt nanoparticles have been successfully fabricated *via* the combination of a mussel-inspired biomimetic polydopamine (PDA)-coating process using electrospun porous polystyrene fibers as templates, a simple solution deposition method and subsequent high-temperature carbonization. This rationally designed porous NCF–Co composite possesses a large surface area and numerous electrochemically active sites, which exhibits synergistically improved catalytic activity for oxygen reduction reactions (ORRs) with a relatively positive onset potential, large current density, as well as superior durability compared with the commercial platinum–carbon (Pt/C) catalyst, making it a promising noble-metal-free catalyst for practical ORR applications.

Introduction

With the increasing demand for clean and sustainable energy, a great deal of effort has been devoted to the exploration of advanced energy conversion and storage systems, such as supercapacitors, lithium-ion batteries, fuel cells and metal–air batteries.[1–3] Among them, fuel cells and metal–air batteries are considered as promising energy conversion devices due to their high efficiency and environmental friendliness, where the oxygen reduction reaction (ORR) plays a critical role on the cathode.[4] Although platinum (Pt)-based materials have been recognized as the most active catalysts for the ORR, the high cost, weak durability, and lack of methanol tolerance largely limit their large-scale applications. To address these problems, noble-metal-free ORR catalysts, *e.g.*, Co or Fe-based catalysts, have been investigated as promising candidates to replace the Pt-based catalysts.[5,6] However, the activity and stability of these materials as ORR catalysts are still unqualified to meet the requirements for practical applications in fuel cells.

In recent years, carbon materials, especially nitrogen (N)-doped carbon materials, have been employed as effective supports in ORR catalysts due to their good catalytic activity, high durability and conductivity.[7] Many studies suggest that incorporation of N into carbon materials can create a delocalized conjugated system between the lone electron pairs of N atoms and the sp^2 graphitic framework, which facilitates faster electron transfer among the catalyst, electrode, and reactant.[8,9] For instance, N-doped graphene/Co_3O_4 composites,[10] N-doped three dimensional (3D) crumpled graphene–CoO hybrids,[11] and flexible N-doped graphene/carbon nanotube/Co_3O_4 paper[12] have been designed and investigated as catalysts for ORRs, showing excellent electrocatalytic performance in alkaline solutions with superior stability. Many sources of N-contained materials can be used for N doping, such as NH_3, pyridine and pyrrole. However, the rigorous synthesis conditions and toxicity of these nitrogen precursors limit their uses in many cases.[8] Therefore, simple synthesis methods using nontoxic N-doping agents are highly desirable.

Dopamine, a kind of biomolecule containing catechol and amine functional groups, has been employed as a straightforward and eco-friendly N-doping agent.[13–15] This is because dopamine can spontaneously self-polymerize on a variety of substrates, and thus the resulted polydopamine (PDA) is proved

[a]State Key Laboratory of Molecular Engineering of Polymers, Department of Macromolecular Science, Fudan University, Shanghai, 200433, P. R. China. E-mail: txliu@fudan.edu.cn

[b]State Key Laboratory for Modification of Chemical Fibers and Polymer Materials, College of Materials Science and Engineering, Donghua University, Shanghai 201620, China. E-mail: 12110440023@fudan.edu.cn

[c]Key Laboratory of New Processing Technology for Nonferrous Metals and Materials, Ministry of Education, College of Materials Science and Engineering, Guilin University of Technology, Guilin, 541004, China

† Electronic supplementary information (ESI) available: Nitrogen adsorption–desorption isotherms of NCF fibers and the corresponding pore size distribution plots; element contents, LSV curves and electron transfer numbers of different NCF fibers; TGA curves of pure PS fibers, PDA particles and PS@PDA composite fibers; relative atomic ratio of N species obtained from the deconvoluted N 1s peaks; TGA curves of NCF–Co composites and XRD patterns of the TGA residue. See DOI: 10.1039/c5ta06217a

to have excellent thermal stability which can be directly converted to N-rich carbonous materials by heat treatment.[16,17] Moreover, PDA shows special adsorption capability toward some metal ions (*e.g.* Fe^{3+}/Fe^{2+}, Co^{3+}/Co^{2+} and Ag^{+}), providing a facile method to immobilize desired metal nanoparticles onto the PDA surface.[18–20]

Electrospinning is a simple and versatile technique for the fabrication of continuous fibers with diameters from the micro- to nano-scale.[21] Electrospun fiber membranes exhibit outstanding properties such as high porosity, large surface area to volume ratio and excellent flexibility, making them ideal candidates for applications as catalysts, sensors, drug carriers, *etc.*[22–25] In our previous study, porous fibers have been obtained by simple selective dissolution or calcination of electrospun precursor fibers, which were demonstrated to show greatly increased surface area and porosity *via* the construction of porous structures.[26–29] Hence, porous polystyrene (PS) fibers with a large surface area and high porosity have been fabricated *via* electrospinning in this work, and employed as the matrix for *in situ* polymerization of dopamine. The self-polymerized PDA-coated PS (PS@PDA) fibers with residual catechol groups were then immersed in $Co(NO_3)_2$ solution to adsorb Co^{2+} ions. Finally, NCF–Co composites of N-doped carbon fibers loaded with Co nanoparticles can be produced through the subsequent annealing process. It is worth mentioning that PDA not only serves as the N source in this work, but also directs the uniform distribution of Co nanoparticles on/in the porous fibers. It is demonstrated that by the rational combination of the unique PDA-derived porous carbon fibers and electrochemically active Co nanoparticles, the obtained NCF–Co composites exhibit excellent catalytic performance toward oxygen reduction reactions, being promising Pt-free ORR catalysts for potential fuel cell applications.

Experimental

Materials

PS ($M_w \approx 25\,000$) was purchased from Sigma-Aldrich. Dopamine hydrochloride (98%) was obtained from Aladdin Chemical Reagent. Tris(hydroxymethyl)aminomethane (TRIS, 99%) and tris(hydroxylmethyl)aminomethane hydrochloride (TRIS·HCl, 99%) were purchased from Alfa Aesar. Cobalt nitrate hexahydrate ($Co(NO_3)_2 \cdot 6H_2O$, 99%) and cobalt nanoparticles (100 nm) were supplied by Sinopharm Chemical Reagent Co., Ltd. Deionized water was used as the solvent for all experiments. All other reagents were of analytical grade and used without further purification.

Preparation of PDA-coated PS fibers

Firstly, PS was dissolved in *N*,*N*-dimethylformamide (DMF) under vigorous stirring at room temperature for 12 h to prepare a 25 wt% homogeneous solution for electrospinning. Then, the solution was loaded into a syringe equipped with a stainless steel needle. During the electrospinning process, a voltage of 12 kV and a feeding rate of 1 mL h^{-1} were applied to a spinneret. Ethanol was used as the liquid collector to obtain hydrophilic porous PS fibers. PDA-coated PS fibers were prepared according to the literature.[23,30] The as-spun PS fibers were immersed in a freshly prepared aqueous solution of dopamine (1 mg mL^{-1} in 10 mM Tris buffer, pH = 8.5) at 50 °C for 5 h. After the reaction, the fibers were thoroughly washed with deionized water several times to remove the non-adhered PDA, and then dried overnight at 60 °C in a vacuum oven.

Preparation of NCF–Co composites

Nanocomposites of N-doped carbon fibers loaded with Co nanoparticles, denoted as NCF–Co, were produced through a simple immersion process followed by subsequent annealing. In a typical procedure, 1 g PDA-coated PS fibers were immersed in 50 mL $Co(NO_3)_2 \cdot 6H_2O$ solution at room temperature for 6 h, followed by drying at 60 °C and calcination under an argon atmosphere at 700 °C for 2 h to remove the PS template and obtain Co decorated N-doped carbon fibers simultaneously. The NCF–Co composites with different loading amounts of Co nanoparticles were fabricated by varying the concentration (*i.e.* 0.2 M, 0.5 M, 0.8 M and 1.0 M) of $Co(NO_3)_2 \cdot 6H_2O$ solution, which were labelled as NCF–Co-0.2 M, NCF–Co-0.5 M, NCF–Co-0.8 M and NCF–Co-1.0 M, respectively. Besides, neat nitrogen-doped carbon fibers (NCFs) obtained under different dopamine concentrations (*i.e.*, 0.5, 1 and 2 mg mL^{-1}) were also prepared using the same method in the absence of $Co(NO_3)_2$ and labelled as NCF-0.5, NCF-1.0 and NCF-2.0, respectively, with the NCF-1.0 component chosen as the optimized sample of neat NCF fibers due to its comprehensive advantages on the specific surface area and N-doping content (Fig. S1 and Table S1†). Moreover, the NCF–Co-0.5 M composite has been selected as the representative sample in comparison with pure NCF fibers for further structural characterization and electrochemical tests. The complete preparation procedure of NCF–Co composites is schematically shown in Fig. 1.

Characterization

The morphology of the samples was observed by using a field-emission scanning electron microscope (FESEM, Ultra 55,

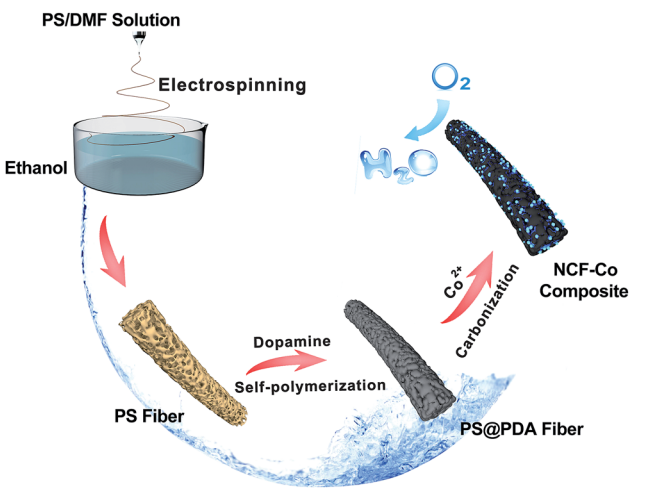

Fig. 1 Schematic illustration of the preparation of NCF–Co composites.

Zeiss). Transmission electron microscopy (TEM) observations were performed using a Tecnai G2 20 TWIN TEM. XRD patterns were obtained on a PANalytical (X'Pert PRO) X-ray diffractometer operated at 40 kV and 40 mA using Cu K_α radiation (λ = 0.1542 nm). Elemental analysis of carbon, hydrogen, nitrogen and cobalt was examined by X-ray photoelectron spectroscopy (XPS) with a VG ESCALAB 220I-XL device. The specific surface area and pore size distribution were measured using a Micromeritics Tristar II-3020 nitrogen adsorption apparatus. TGA analysis was carried out on a Mettler Toledo TGA1 instrument under constant air flow with a heating rate of 10 °C min^{-1}.

Electrochemical measurements

The ORR activity of all samples was tested in a conventional three-electrode cell using a CHI 600 electrochemical workstation (Shanghai Chenhua Instrument Co., China) equipped with a rotating electrode setup. An Ag/AgCl electrode and Pt wire were used as the reference electrode and the counter-electrode, respectively. The glassy carbon electrode (GCE) and rotating disk electrode (RDE) loaded with various catalysts were used as the working electrodes. To prepare a homogeneous catalyst ink, 10 mg of the as-synthesized catalyst was dispersed in 5 mL mixed solvent of water–DMF (v/v = 1/1) along with 0.1 mL of Nafion solution (5 wt%, Sigma-Aldrich) and sonicated for about 2 h. Then, an appropriate amount of this suspension was transferred onto the GCE/RDE electrode to be fully dried. The loading amount of the catalyst was set at 10 μg on the GCE for cyclic voltammetry (CV) measurements, and 20 μg on the RDE for linear sweep voltammetry (LSV) and chronoamperometry measurements. All electrochemical tests were conducted at room temperature in 0.1 M N_2 or O_2-saturated KOH aqueous solution.

The electron transfer number (n) and kinetic current density (J_k) were investigated based on the Koutecky–Levich (K–L) equation:

$$\frac{1}{J} = \frac{1}{J_L} + \frac{1}{J_k} = \frac{1}{B\omega^{1/2}} + \frac{1}{J_k} \quad (1)$$

$$B = 0.2nFC_o(D_o)^{2/3}\nu^{-1/6} \quad (2)$$

where J is the measured current density, J_k is the kinetic current density, J_L is the diffusion current density, ω is the electrode rotation rate, F is the Faraday constant (96 485 C mol^{-1}), C_o is the bulk concentration of O_2 (1.2×10^{-6} mol cm^{-3}), D_o is the diffusion coefficient of O_2 (1.9×10^{-5} cm^2 s^{-1}), and ν is the kinetic viscosity of the electrolyte (0.01 cm^2 s^{-1}). Here, the constant 0.2 is adopted when the rotating rate is expressed in rpm.

Results and discussion

Morphology of porous PS@PDA fibers

PS fibers were prepared *via* electrospinning of PS/DMF solution using ethanol as the liquid collector.[23,30] Porous microstructures are effectively induced by phase separation which results from the evaporation of ethanol during the reception process.[31] As shown in Fig. 2a, uniform pore structures can be observed on and inside the as-obtained PS fibers with diameters ranging in 2–4 μm. The porous PS fibers form a loose cotton-like clump in ethanol (Fig. 2b) which exhibit relatively good wettability, thus ensuring post-coating of PDA in aqueous medium. The PS fibers were then immersed in the Tris-buffer solution of dopamine for 5 h. After the self-polymerization of dopamine on/in the porous fibers, the color of the PS lump changes from white to black (Fig. 2a), indicating the successful formation of the PDA layer. Meanwhile, as verified by FESEM observations (Fig. 2c and d), the PS@PDA fibers show a smooth surface which is attributed to the uniformly coated PDA layer with the porous channels inside the fibers which are completely retained.

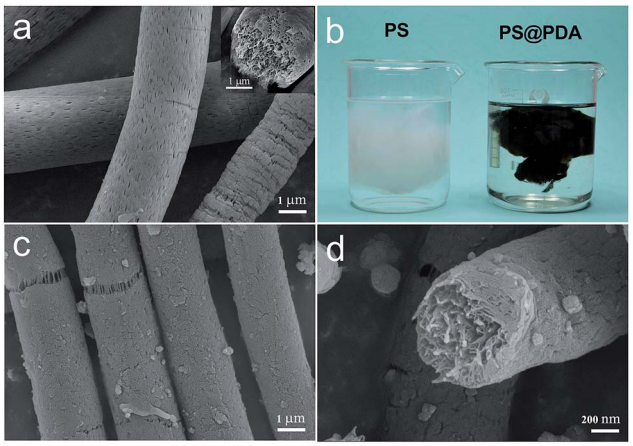

Fig. 2 FESEM image of PS fibers (a), digital photos of porous PS fibers in ethanol before and after PDA coating (b), and FESEM images of PDA-coated PS fibers (c and d).

Characterization of NCF–Co composites

PS@PDA fibers possess plenty of active catechol groups, which can form covalent bonds with molecules containing primary amine groups, as well as coordination bonds with specific metal ions.[20] Based on the unique properties, porous carbon fibers loaded with Co nanoparticles are obtained *via* the annealing of Co^{2+} absorbed PDA@PS fibers. Due to the full decomposition of PS above 500 °C in an inert environment (Fig. S2†), the obtained carbon fibers are supposed to be yielded mainly from the PDA coating rather than the PS backbone, thus achieving further increased surface area. The morphology of the as-prepared carbon fibers decorated with/without Co nanoparticles was characterized by FESEM. It can be seen that obvious porous channels in NCF fibers are wrapped by a relatively dense shell derived from the outer PDA coating, manifesting a core–shell structure as shown in Fig. 3a and b. The Brunauer–Emmett–Teller (BET) surface area determined by the typical nitrogen (77 K) adsorption/desorption isotherms of the NCF fibers is 356 m^2 g^{-1} (Fig. S1a†), much higher than those of the previously reported solid or porous carbon fibers.[32,33] Furthermore, the Barrett–Joyner–Halenda (BJH) desorption pore size of NCF fibers is mainly distributed in the range of 20–70 nm (Fig. S1b†), which provides abundant space for the encapsulation of metal nanoparticles. As expected, FESEM images of NCF–Co

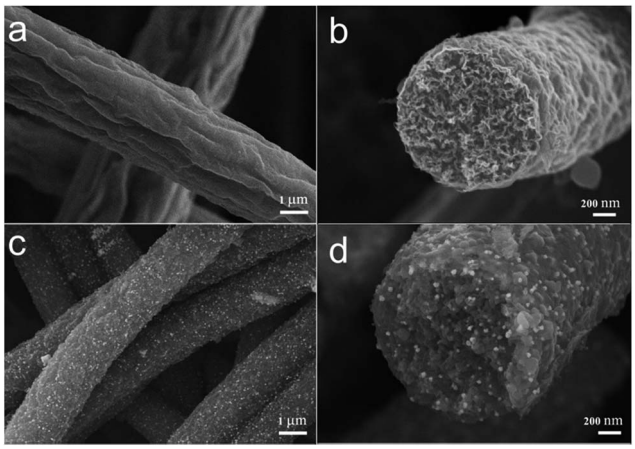

Fig. 3 FESEM images of porous NCF fibers (a and b), and NCF–Co composites (c and d).

composites demonstrate that Co nanoparticles are uniformly distributed on both the shell and inside of NCF fibers (Fig. 3c and d). In addition, the porous structure of NCF fibers is clearly observed from the TEM image (Fig. 4a), in accordance with the FESEM observations. The TEM image of the NCF–Co composite (Fig. 4b) further reveals the uniform decoration of Co nanoparticles in NCF fibers with a mean size of 30 nm, indicating that the porous structure of NCF fibers can effectively prevent Co nanoparticles from agglomeration. Therefore, it is favorable for fast electron transport between the carbon fiber matrix and Co nanoparticles, thus leading to efficient electrochemical performance.[34,35]

The structures of NCF fibers and NCF–Co composite were further investigated by XRD, as shown in Fig. 5a. For pure NCF fibers, a broad diffraction peak at $2\theta = 24.3°$ is attributed to the amorphous carbon after carbonization of PDA@PS fibers. The well-defined peaks at $2\theta = 44.3°$, 51.6°, and 75.8° of NCF–Co composites are in good agreement with the (111), (200), and (220) reflection planes of cobalt (JCPDS card 15-0806), confirming the presence of metallic cobalt in the NCF–Co composite. XPS was used to analyze the elemental composition of NCF fibers and NCF–Co composites. As shown in Fig. 5b, the survey spectrum indicates the existence of C, N, O and Co elements, confirming that nitrogen and cobalt are successfully incorporated into carbon fibers. The high-resolution XPS spectrum of N 1s (Fig. 5c) reveals the doping of pyridinic-*N* (398.3

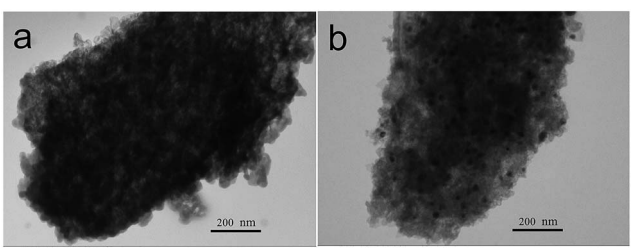

Fig. 4 TEM images of porous NCF fibers (a), and NCF–Co composites (b).

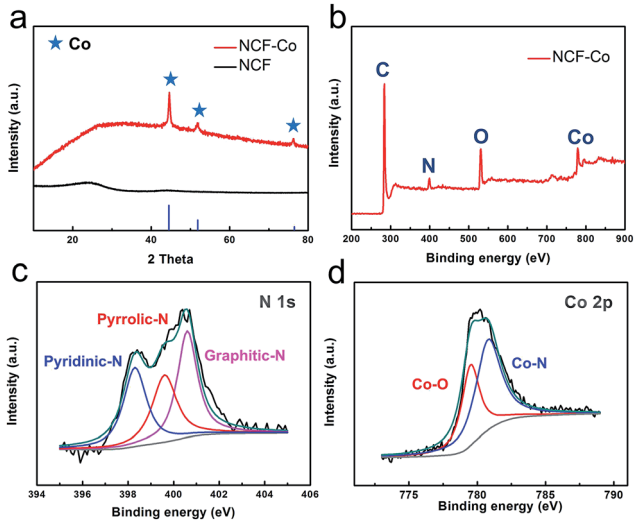

Fig. 5 (a) XRD patterns of NCF fibers and NCF–Co composites, (b) XPS spectra of NCF–Co composites, and the corresponding high-resolution XPS spectra of N 1s (c) and Co 2p (d).

eV), pyrrolic-*N* (399.6 eV) and graphitic-*N* (400.6 eV) species in the NCF–Co composite, with the relative ratio of N species shown in Table S2.† Graphitic-*N* and pyridinic-*N* are reported to be favourable for ORRs *via* improving the limited current density and onset potential.[35,36] Thus, the carbon matrix enriched with graphitic-*N* and pyridinic-*N* in this work is expected to play an important role in enhancing the ORR activity of NCF–Co composites. Besides, the Co 2p spectrum can be further deconvoluted into two different peaks (Fig. 5d) at binding energies of 780.5 eV and 779.4 eV, corresponding to the Co–N and Co–O groups, respectively. The presence of Co–O moieties may be ascribed to the slight oxidation of metallic cobalt while the dominated Co–N groups indicate the coordination between Co and N, which was reported to greatly contribute to the electrocatalytic activity of N-doped Co/carbon composites.[37]

Electrochemical characterization of NCF–Co composite catalysts

The catalytic activity of NCF–Co composites and NCF fibers toward ORRs was first evaluated by CV in N_2-saturated (dotted line) and O_2-saturated (solid line) 0.1 M KOH aqueous solution at a scan rate of 10 mV s^{-1} (Fig. 6a). Distinct oxygen reduction peaks can be observed for both NCF fibers and NCF–Co composite catalysts in O_2-saturated KOH solution, implying their pronounced catalytic activity for ORRs. Compared to NCF fibers, greatly enhanced catalytic performance with more positive E_{peak} potential (−0.17 V) and larger current density is obtained for NCF–Co composites. Moreover, the E_{peak} potential at −0.17 V is very close to that of the N-doped graphene supported Co complex reported recently,[38] and outperforms most of the previous Co/carbon based catalysts as shown in Table 1. To further investigate the ORR catalytic activity of NCF and NCF–Co catalysts, LSV measurements were carried out at various

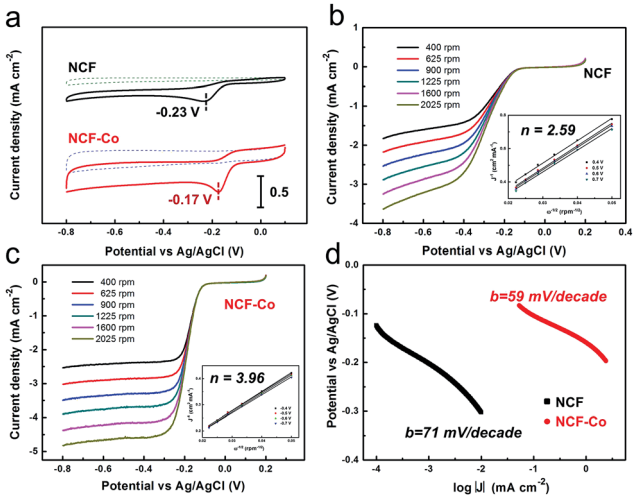

Fig. 6 (a) CV curves of NCF fibers and NCF–Co composite in O_2-saturated (solid line) and N_2-saturated (dashed line) 0.1 M KOH solution at a scan rate of 10 mV s^{-1}. Rotating-disk voltammograms of NCF fibers (b) and NCF–Co composites (c) in O_2-saturated 0.1 M KOH with a sweep rate of 5 mV s^{-1} at various rotation speeds (The insets show the corresponding Koutecky–Levich plots at different potentials). (d) Tafel plots of NCF fibers and NCF–Co composites derived from the corresponding RDE data.

rotation speeds in O_2-saturated 0.1 M KOH solution (Fig. 6b and c and S3†). As shown in Fig. 6b and c, the current density of both NCF and NCF–Co modified RDEs increases with increasing rotation rate from 400 to 2025 rpm, which can be ascribed to the shortened diffusion distance for electron transfer at high speed.[11] The insets of Fig. 6b and c show the corresponding Koutecky–Levich (K–L) plots (J^{-1} *vs.* $\omega^{-1/2}$) at various potentials, with the electron transfer number (n) calculated to be 3.96 and 2.59 for NCF–Co and NCF catalysts, respectively, indicating that the NCF–Co electrode favors a more efficient $4e^-$ oxygen reduction process, while the NCF electrode involves a $2e^-$ reduction process with H_2O_2 as the intermediate agent. Besides, Tafel plots of NCF and NCF–Co catalysts derived from the corresponding RDE data at 1600 rpm are shown in Fig. 6d. The linear part of the Tafel plots is fitted to the Tafel equation ($\eta = b \log j + a$, where j is the current density and b is the Tafel slope), yielding Tafel slopes of about 59 and 71 mV dec^{-1} for NCF–Co composites and NCF fibers, respectively, which reconfirmed the improved catalytic activity for ORRs after the incorporation of Co nanoparticles.

Based on the CV and LSV measurements, it is evident that Co incorporation can greatly improve the ORR catalytic activity of NCF fibers. Therefore, NCF–Co composites with different loading amounts of Co nanoparticles were fabricated. As shown in Fig. 7a–c, Co nanoparticles with increased size and density are uniformly distributed on/in NCF fibers with the concentration of $Co(NO_3)_2$ increases from 0.2 M to 0.8 M. Further increasing the concentration of the cobalt precursor to 1.0 M, severe aggregation of Co nanoparticles has been observed on the fiber surface (Fig. 7d), which may block the pores in NCF fibers and affect the ORR performance. In order to further explore the textural information of NCF–Co composites with different uploading amounts of Co nanoparticles, BET analyses were carried out as shown in Fig. 7e and f. NCF–Co-0.2 M, NCF–Co-0.5 M and NCF–Co-0.8 M composites show relatively high specific surface areas of 339, 347 and 327 m^2 g^{-1}, respectively, whereas the NCF–Co-1.0 M composite shows a reduced surface area of 273 m^2 g^{-1} due to the severe aggregation of Co nanoparticles. The corresponding pore size distribution plots demonstrate that all the NCF–Co composites possess wider pore size distributions than that of pure NCF fibers due to the introduction of Co nanoparticles. The high surface area and mesoporous architecture of the composites are favorable for the easier accessibility of electrolyte and faster electron transfer, thus resulting in greatly enhanced electrochemical activity. Additionally, TGA was conducted in air atmosphere to quantitatively determine the content of Co nanoparticles in NCF–Co composites. As shown in Fig. S4a,† a distinctive weight increment can be observed at 200–300 °C, which is ascribed to the oxidation of metallic Co. After the TGA experiments, the residue at 700 °C in air is proved to be Co_3O_4 *via* XRD measurements (Fig. S4b†). Thus, the loading amount of Co nanoparticles in NCF–Co-0.2 M, NCF–Co-0.5 M, NCF–Co-0.8 M and NCF–Co-1.0 M composites is calculated to be 9 wt%, 16 wt%, 37 wt% and 50 wt%, respectively.

Table 1 Comparison of the catalytic activity data (V *vs.* Ag/AgCl) with Co/carbon based ORR catalysts reported previously

Catalysts	Electrolyte	Reduction peak	Onset potential	Half-wave potential	References
$[CoN_4]_3$/C	0.1 M KOH	−0.26	−0.14	N/A	4
Co/N/reduced graphene oxide (NH_3)	0.1 M KOH	−0.24	−0.11	−0.17	5
Co/N-doped carbon nanotubes	0.1 M KOH	−0.23	N/A	N/A	7
Co–NMCV[a]	0.1 M KOH	−0.22	−0.13	−0.19	8
NCo–GS[b]	0.1 M KOH	−0.21	−0.08	N/A	10
Co_3O_4/N-MG[c]	0.1 M KOH	−0.20	−0.09	N/A	9
Co–N–GN[d]	0.1 M KOH	−0.18	−0.10	−0.16	12
N–CG–CoO[e]	0.1 M KOH	N/A	−0.12	−0.21	11
NCF–Co	0.1 M KOH	−0.17	−0.09	−0.18	This work

[a] Co–NMCV: cobalt and nitrogen co-doped mesoporous carbon vesicles. [b] NCo–GS: graphitic C_3N_4 embedded CoO particle/grapheme sheet hybrids. [c] Co_3O_4/N-MG: nitrogen doped mesoporous graphene/Co_3O_4 composite. [d] Co–N–GN: nanosheet-like cobalt–nitrogen–graphene. [e] N–CG–CoO: nitrogen-doped crumpled graphene/cobalt oxide hybrids.

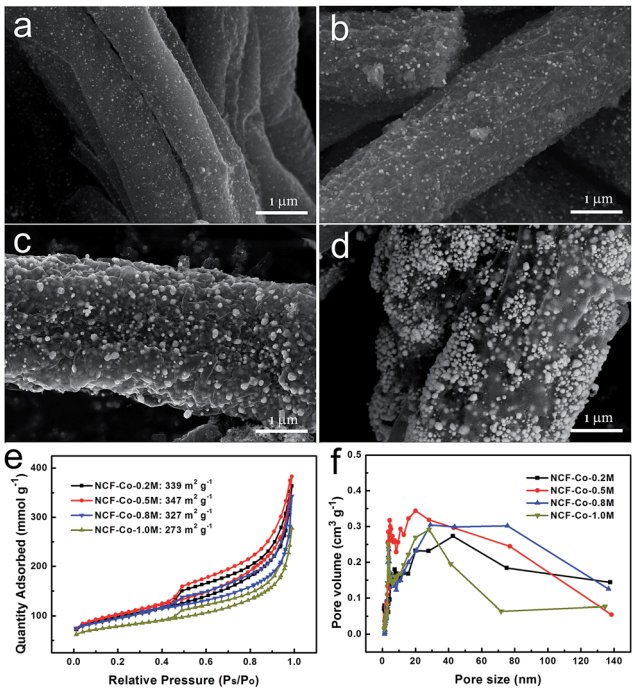

Fig. 7 FESEM images of NCF–Co-0.2 M (a), NCF–Co-0.5 M (b), NCF–Co-0.8 M (c), and NCF–Co-1.0 M (d) composites. Nitrogen adsorption–desorption isotherms of NCF–Co composites (e) and the corresponding pore size distribution plots (f).

To investigate the electrochemical catalytic performance of NCF–Co composites with different contents of Co nanoparticles, the CV measurement in O_2-saturated 0.1 M KOH was conducted (Fig. 8a). It can be seen that all NCF–Co composites exhibit excellent catalytic activity for ORRs with identical E_{peak} potentials at −0.17 V, while their current densities vary with the loading contents of Co nanoparticles. Generally, increasing the loading content of Co nanoparticles may lead to more reactive sites, thus resulting in higher E_{peak} current density for NCF–Co-0.8 M composites compared to those of NCF–Co-0.2 M and NCF–Co-0.5 M composites. However, excessive Co nanoparticles on/in NCF fibers easily form severe aggregations to block the electrochemically active sites, leading to degraded catalytic performance for the NCF–Co-1.0 M composite. Fig. 8b shows the ORR polarization curves of all NCF–Co composites. It was observed that the onset potential of all the samples is nearly the same that reaches up to −0.09 V. As expected, the NCF–Co-0.8 M composite exhibits a larger current density of 4.57 mA cm^{-2} at −0.8 V, which is better than those of NCF–Co-0.2 M (3.44 mA cm^{-2}), NCF–Co-0.5 M (4.29 mA cm^{-2}) and NCF–Co-1.0 M (3.87 mA cm^{-2}) composites. Moreover, the electron transfer numbers of the composite catalysts are calculated to be 3.55–3.96 (Fig. 8c), which reveals that the electrocatalytic process of all NCF–Co composites follows a one-step four-electron pathway for ORRs. In addition, comparisons of different catalysts involving pure NCF, Co nanoparticles, NCF–Co-0.8 M composites and commercial Pt/C were also performed. As shown in Fig. 8d, lower onset potential and larger current density are observed for NCF–Co-0.8 M composites compared to those of neat NCF and Co nanoparticles, providing strong evidence for the synergistic effect between NCF and Co nanoparticles toward ORRs. Moreover, the NCF–Co-0.8 M catalyst exhibits a cathodic shift of only 50 mV at the onset potential compared to that of the commercial Pt/C catalyst, which is superior to most Co-based ORR catalysts (Table 1).

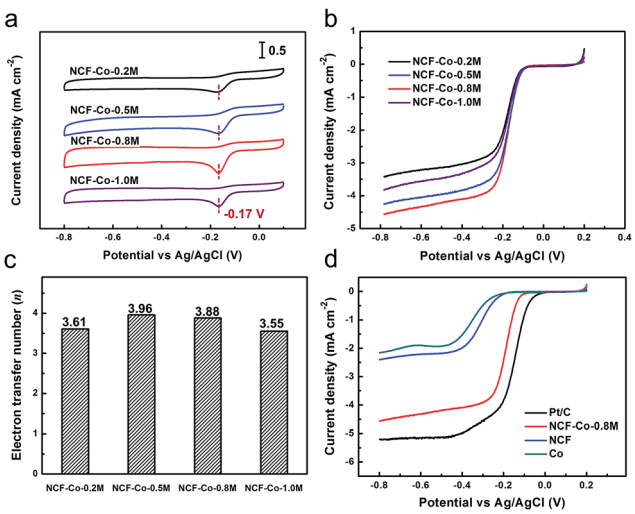

Fig. 8 (a) CV curves of different NCF–Co composites in O_2-saturated 0.1 M KOH solution. Scan rate: 10 mV s^{-1}. (b) LSV curves of different NCF–Co composites. Scan rate: 5 mV s^{-1}, rotating rate: 1600 rpm. (c) Electron transfer numbers of different NCF–Co composites derived from their corresponding LSV data. (d) ORR polarization curves of NCF fibers, NCF–Co-0.8 M, Co nanoparticles, and the commercial Pt/C catalysts in O_2-saturated 0.1 M KOH solution. Scan rate: 5 mV s^{-1}, rotating rate: 1600 rpm.

Since methanol tolerance is one of the major concerns in fuel cells, chronoamperometry was used to characterize the stability of the electrodes at a constant voltage of −0.4 V in O_2-saturated 0.1 M KOH aqueous solution. As shown in Fig. 9a, after the addition of 5 M methanol at 100 s, a drastic current decrease is observed in the ORR current of the Pt/C electrode, indicating the occurrence of the methanol oxidation reaction. In contrast, the NCF–Co composite exhibits excellent selectivity with no visible response to methanol oxidation, presenting a much better methanol tolerance than the commercial Pt/C. The durability of NCF–Co and Pt/C catalysts was measured by holding them at −0.4 V for 10 000 s in O_2-saturated 0.1 M KOH

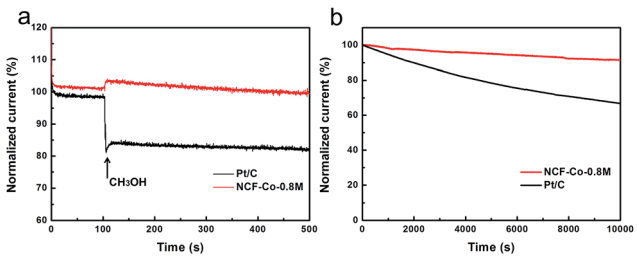

Fig. 9 Chronoamperometric responses of NCF–Co-0.8 M and Pt/C catalysts: (a) methanol crossover test by addition of methanol to the electrochemical cell at 100 s; (b) stability test for 10 000 s.

solution (Fig. 9b). Chronoamperometric response of the NCF–Co catalyst exhibits a current retention of 90% after 10 000 s. In contrast, more than 30% reduction in the corresponding current is observed for the Pt/C electrode. All these results confirm the high stability and excellent methanol crossover immunity of the NCF–Co catalyst, and highlight its great potential in methanol and alkaline fuel cell applications.

Conclusions

In summary, a new strategy is proposed for fabricating a high-performance ORR electrocatalyst composed of NCF and Co nanoparticles *via* biologically inspired polymerization and thermal treatment. Notably, the PDA@PS porous fiber provides a large surface area and stable anchoring sites for the uniform adsorption of Co ions, followed by calcination to remove the PS template and realize N-doping simultaneously. The obtained NCF–Co composites exhibit excellent ORR catalytic activity with a relatively positive onset potential and high current density through a four-electron reduction mechanism, which is comparable to the commercial Pt/C electrode. Furthermore, the NCF–Co composite shows superior durability and tolerance to methanol crossover effects over the Pt/C catalyst, being a promising Pt-free ORR catalyst for fuel cell and water splitting applications.

Acknowledgements

The authors are grateful for the financial support from the National Natural Science Foundation of China (51125011, 51373037, and 51433001), Guangxi Small Highland Innovation Team of Talents in Colleges and Universities, Guangxi Funds for Specially appointed Expert, and Guangxi Natural Science Foundation of China (No. 2014GXNSFAA118321).

Notes and references

1 M. Winter and R. J. Brodd, *Chem. Rev.*, 2004, **104**, 4245–4270.
2 A. A. Gewirth and M. S. Thorum, *Inorg. Chem.*, 2010, **49**, 3557–3566.
3 A. Kudo and Y. Miseki, *Chem. Soc. Rev.*, 2009, **38**, 253–278.
4 F. Jaouen, E. Proietti, M. Lefèvre, R. Chenitz, J. Dodelet, G. Wu, H. T. Chung, C. M. Johnston and P. Zelenay, *Energy Environ. Sci.*, 2011, **4**, 114–130.
5 Q. G. He, Q. Li, S. Khene, X. Ren, F. E. López-Suárez, D. Lozano-Castelló, A. Bueno-López and G. Wu, *J. Phys. Chem. C*, 2013, **117**, 8697–8707.
6 G. Wu, K. L. More, C. M. Johnston and P. Zelenay, *Science*, 2011, **332**, 443–447.
7 L. Dai, D. W. Chang, J. B. Baek and W. Lu, *Small*, 2012, **8**, 1130–1166.
8 H. Wang, T. Maiyalagan and X. Wang, *ACS Catal.*, 2012, **2**, 781–794.
9 J. J. Xiao, X. J. Bian, L. Liao, S. Zhang, C. Ji and B. H. Liu, *ACS Appl. Mater. Interfaces*, 2014, **6**, 17654–17660.
10 Y. Y. Liang, Y. G. Li, H. L. Wang, J. G. Zhou, J. Wang, T. Regier and H. J. Dai, *Nat. Mater.*, 2011, **10**, 780–786.
11 S. Mao, Z. H. Wen, T. Z. Huang, Y. Hou and J. H. Chen, *Energy Environ. Sci.*, 2014, **7**, 609–616.
12 S. S. Li, H. P. Cong, P. Wang and S. H. Yu, *Nanoscale*, 2014, **6**, 7534–7541.
13 Y. H. Lee, H. Lee, Y. B. Kim, J. Kim, T. Hyeon, H. Park, P. B. Messersmith and T. G. Park, *Adv. Mater.*, 2008, **20**, 4154–4157.
14 S. M. Kang, N. S. Hwang, J. Yeom, S. Y. Park, P. B. Messersmith, I. S. Choi, R. Langer, D. G. Anderson and H. Lee, *Adv. Funct. Mater.*, 2012, **22**, 2949–2955.
15 Y. H. Li, M. Zhou, C. Z. Geng, F. Chen and Q. Fu, *Chin. J. Polym. Sci.*, 2014, **32**, 1724–1736.
16 R. Liu, S. M. Mahurin, C. Li, R. R. Unocic, J. C. Idrobo, H. J. Gao, S. J. Pennycook and S. Dai, *Angew. Chem., Int. Ed.*, 2011, **50**, 6799–6802.
17 Z. Y. Ma, X. Jia, J. M. Hu and B. Dai, *RSC Adv.*, 2014, **4**, 1853–1856.
18 J. J. Zhou, B. Duan, Z. Fang, J. B. Song, C. X. Wang, P. B. Messersmith and H. W. Duan, *Adv. Mater.*, 2014, **26**, 701–705.
19 V. Bambagioni, C. Bianchini, J. Filippi, A. Lavacchi, W. Oberhauser, A. Marchionni, S. Moneti, F. Vizza, R. Psaro and V. Dal Santo, *J. Power Sources*, 2011, **196**, 2519–2529.
20 H. W. Yang, Y. Lan, W. Zhu, W. N. Li, D. Xu, J. C. Cui, D. Z. Shen and G. T. Li, *J. Mater. Chem.*, 2012, **22**, 16994–17001.
21 R. Aikifa, J. Q. Wang, S. Yang, Y. Si and B. Ding, *Carbon Lett.*, 2014, **15**, 1–14.
22 Y. E. Miao and T. X. Liu, *Acta Polym. Sin.*, 2012, **8**, 801–811.
23 J. H. Kong, X. Y. Yao, Y. F. Wei, C. Y. Zhao, J. M. Ang and X. H. Lu, *RSC Adv.*, 2015, **5**, 13315–13323.
24 A. Greiner and J. H. Wendorff, *Angew. Chem., Int. Ed.*, 2007, **46**, 5670–5703.
25 L. Zhang, Y. Guo, W. H. Chi, H. G. Shi, H. Q. Ren and T. Y. Guo, *Chin. J. Polym. Sci.*, 2014, **32**, 1469–1478.
26 Y. P. Huang, Y. E. Miao, S. S. Ji, W. W. Tjiu and T. X. Liu, *ACS Appl. Mater. Interfaces*, 2014, **6**, 12449–12456.
27 Y. E. Miao, W. Fan, D. Chen and T. X. Liu, *ACS Appl. Mater. Interfaces*, 2013, **5**, 4423–4428.
28 Y. E. Miao, J. J. Yan, Y. P. Huang, W. Fan and T. X. Liu, *RSC Adv.*, 2015, **5**, 26189–26196.
29 Y. P. Huang, Y. E. Miao, H. Y. Lu and T. X. Liu, *Chem.–Eur. J.*, 2015, **21**, 10100–10108.
30 J. H. Kong, C. Y. Zhao, Y. F. Wei, S. L. Phua, Y. L. Dong and X. H. Lu, *J. Mater. Chem. A*, 2014, **2**, 15191–15199.
31 Y. Q. Wu and R. L. Clark, *J. Colloid Interface Sci.*, 2007, **310**, 529–535.
32 J. Wu, H. W. Park, A. P. Yu, D. Higgins and Z. W. Chen, *J. Phys. Chem. C*, 2012, **116**, 9427–9432.
33 S. G. Wang, Z. T. Cui and M. Cao, *Chem.–Eur. J.*, 2015, **21**, 2165–2172.
34 Y. Xiao, C. G. Hu, L. T. Qu, C. W. Hu and M. H. Cao, *Chem.–Eur. J.*, 2013, **19**, 14271–14278.
35 Y. H. Su, Y. H. Zhu, H. L. Jiang, J. H. Shen, X. L. Yang, W. J. Zou, J. D. Chen and C. Z. Li, *Nanoscale*, 2014, **6**, 15080–15089.

36 S. Jiang, C. Z. Zhu and S. J. Dong, *J. Mater. Chem. A*, 2013, **1**, 3593–3599.
37 Y. Wang, Y. Nie, W. Ding, S. G. Chen, K. Xiong, X. Q. Qi, Y. Zhang, J. Wang and Z. D. Wei, *Chem. Commun.*, 2015, **51**, 8942–8945.
38 Y. Gartia, C. M. Felton, F. Watanabe, P. K. Szwedo, A. S. Biris, N. Peddi, Z. A. Nima and A. Ghosh, *ACS Sustainable Chem. Eng.*, 2015, **3**, 97–102.